

Damage mechanisms in the dynamic fracture of nominally brittle polymers

Davy Dalmas · Claudia Guerra ·
Julien Scheibert · Daniel Bonamy

Received: 19 November 2012 / Accepted: 19 March 2013 / Published online: 9 April 2013
© Springer Science+Business Media Dordrecht 2013

Abstract Linear elastic fracture mechanics provides a consistent framework to evaluate quantitatively the energy flux released to the tip of a growing crack. Still, the way in which the crack selects its velocity in response to this energy flux remains far from completely understood. To uncover the underlying mechanisms, we experimentally studied damage and dissipation processes that develop during the dynamic failure of polymethylmethacrylate, classically considered as the archetype of brittle amorphous materials. We evidenced a well-defined critical velocity along which failure switches from nominally-brittle to quasi-brittle, where crack propagation goes hand in hand with the nucleation and growth of microcracks. Via post-mortem analysis of the fracture surfaces, we were able to reconstruct the complete spatiotemporal microcracking dynamics with micrometer/nanosecond resolution. We demonstrated that the true local propagation speed of individual crack fronts is limited to a fairly low value,

which can be much smaller than the apparent speed measured at the continuum-level scale. By coalescing with the main front, microcracks boost the macroscale velocity through an acceleration factor of geometrical origin. We discuss the key role of damage-related internal variables in the selection of macroscale fracture dynamics.

Keywords Dynamic fracture · Amorphous polymers · Fracture energy · Fractography · High-deformation rate · Microcracks · PMMA

1 Introduction

Dynamic crack propagation drives catastrophic material failure and is usually described using the linear elastic fracture mechanics (LEFM) framework (Freund 1990; Ravi-Chandar 2004). This theory considers the straight propagation of a single smooth crack and assumes all energy dissipating processes to be entirely localized in a small zone at the crack tip, so called fracture process zone (FPZ). Crack growth velocity v is then selected by the balance between the mechanical energy that flows within the FPZ per time unit and the dissipated energy within the FPZ over the same time unit. This yields (Freund 1990):

$$\Gamma \simeq (1 - v/C_R) K^2(c)/E, \quad (1)$$

where C_R and E are the Rayleigh wave speed and the Young modulus of the material, respectively, Γ is the

D. Dalmas
Unité Mixte CNRS/Saint-Gobain, Surface du Verre et Interfaces, 39 Quai Lucien Lefranc,
93303 Aubervilliers Cedex, France

C. Guerra · J. Scheibert · D. Bonamy (✉)
CEA, IRAMIS, SPCSI, Group Complex Systems and Fracture, 91191 Gif sur Yvette, France
e-mail: Daniel.Bonamy@cea.fr

J. Scheibert
Laboratoire de Tribologie et Dynamique des Systèmes, CNRS, Ecole Centrale de Lyon, 36 Avenue Guy de Collongue, 69134 Ecully Cedex, France

fracture energy, and $K(c)$ is the Stress Intensity Factor (SIF) for a quasi-static crack of length c . K only depends on the applied loading and the cracked specimen geometry, and entirely characterizes the stress field in the vicinity of the crack front.

Linear elastic fracture mechanics predictions agree well with observations as long as the crack growth is sufficiently slow (Bergkvist 1974). However, large discrepancies are reported at high speed (Ravi-Chandar 2004; Bouchbinder et al. 2010). In particular, the maximal crack speeds attained experimentally in amorphous materials are far smaller (typically by a factor of two) than the limiting speed C_R predicted by Eq. 1.

The existence of a micro-branching instability (Fineberg et al. 1992) at a critical velocity v_b (typically of the order of $0.35\text{--}0.4C_R$) permits to explain part of this discrepancy: Beyond v_b , the crack front splits into a multiple crack state that cannot be described by Eq. 1 anymore. However, it is commonly stated (Sharon and Fineberg 1999) that LEFM works well below v_b , or more generally when microbranching instabilities are absent. As a matter of fact, most recent works focused on failure regimes beyond v_b (see e.g. Gumbusch et al. 1997; Adda-Bedia et al. 1999; Henry and Levine 2004; Bouchbinder et al. 2005; Spatschek et al. 2006; Henry 2008). Still, several observations reported at lower speeds remain puzzling. In particular, even for velocities much lower than v_b , the measured dynamic fracture energy is generally found to be much higher than that at crack initiation (Sharon and Fineberg 1999; Kalthoff et al. 1976; Rosakis et al. 1984; Fond and Schirrer 2001).

The experiments reported here were designed to better understand the mechanisms that select crack velocity in dynamic fracture. In this context, we developed an experimental setup (presented in Sect. 2) that permits to characterize over a wide range of crack speeds, in particular speeds below v_b , the dissipative and damage processes that develop in polymethylmethacrylate (PMMA), classically considered as the archetype of brittle amorphous materials. This setup allowed us to evidence a novel critical velocity, smaller than v_b , beyond which crack propagation goes hand in hand with the nucleation and growth of microcracks ahead of the main crack front (Sect. 3). Via accurate *post-mortem* analysis of the patterns left on fracture surfaces, we were able to reconstruct the full spatio-temporal dynamics of these microfailure events (Sect. 4). Their statistics and their dependency with crack tip loading

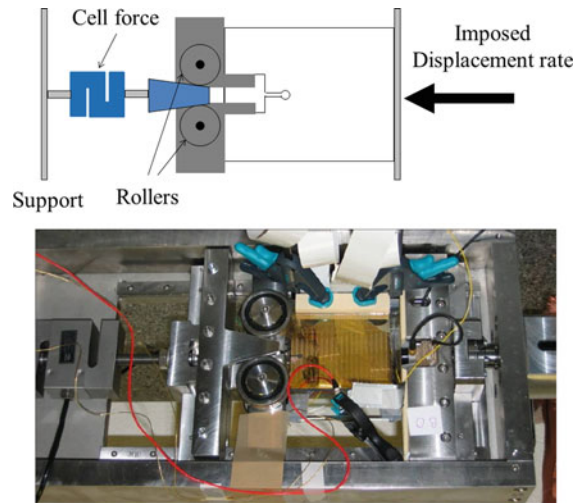


Fig. 1 Sketch (*top*) and photo (*bottom*) of the experimental setup

have been characterized (Sect. 5). In Sect. 6, we will show how microcracking acts and selects the apparent velocity measured at the continuum-level scale.

2 Experimental setup

Fracture tests were performed in the wedge splitting geometry (Bruhwiler and Wittmann 1990; Karihaloo and Xiao 2001) depicted in Fig. 1. Specimens were prepared from PMMA parallelepipeds of size $140 \times 125 \times 15 \text{ mm}^3$ in the propagation (x -axis), loading (y -axis), and thickness (z -axis) directions, respectively. Table 1 gives the main characteristics of the PMMA used in this study. Subsequently, a notch was shaped (1) by cutting a $25 \times 25 \text{ mm}^2$ rectangle from the middle of one of the $125 \times 15 \text{ mm}^2$ edges; and (2) by subsequently adding a 10-mm groove deeper into the specimen. Two steel blocks equipped with rollers were then placed on both sides of this notch and the specimen was loaded by pushing a wedge (semi-angle of 15°) at a small constant velocity ($40 \mu\text{m/s}$) between these two blocks. This permits (1) to spread the loading force over a large contact area and prevent any plastic deformation of PMMA at the loading contacts; and (2) to suppress friction in the system. As a result, the vicinity of the crack tip can be assumed to be the sole dissipation source for mechanical energy in the system.

In such a wedge splitting geometry, the SIF decreases with crack length. To obtain dynamic failure, we then introduced a circular hole of tunable diameter from 2 to 8 mm at the tip of the seed crack. This hole blunts

Table 1 Mechanical properties of the PMMA used in our fracture experiments

	E (GPa)	ν	Density (kg/dm ³)	C_d (m/s)	C_s (m/s)	C_R (m/s)
PMMA	2.8 ± 0.2	0.36 ± 0.08	1.18 ± 0.02	2010 ± 60	950 ± 10	880 ± 30

E and ν denote the Young modulus and the Poisson ratio, respectively. C_D , C_S , and C_R denote the speeds of dilational, Rayleigh waves respectively

the seed crack and delays the propagation onset. This increases the mechanical energy stored in the sample at the onset of crack propagation. It allowed us to widen the range of SIF (from 0.9 to 4.5 MPa $\sqrt{\text{m}}$) and that of crack velocity (from 75 m/s $\approx 0.08C_R$ to 500 m/s $\approx 0.57C_R$) accessible in the experiments.

The apparatus used to carry out the experiments is homemade (Fig. 1). One side of the machine is fixed while the other moves via a stepper motor (Oriental motor EMP400 Series) allowing incremental displacements as small as 40 nm. The compressive force is measured, up to 20 kN via a S-type Vishay load cell 363 Series. In all performed tests, both the displacement and the force are recorded via a computer with a time resolution of 1 s. In particular, the value of the applied force at propagation onset is recorded and later used in the finite element analyses described thereafter.

To measure the instantaneous crack velocity, we used a modified version of the electrical resistance grid technique (Cotterell 1968; Anthony et al. 1970; Boudet et al. 1996; Fineberg et al. 1992). A series of 90 parallel conductive lines (2.4-nm-thick Cr layer covered with 23-nm-thick Au layer) were deposited on one of the two $140 \times 125 \text{ mm}^2$ sides of the specimen using magnetron sputtering deposition through a polymer mask glued on the sample surface. Stripes width and length are 500 μm and 100 mm, respectively, and they are separated by gaps of 500 μm . Once the sample is installed in the compression machine, each line is connected in series with a resistor of 30 k Ω —this value was chosen to be extremely high with respect to that of the strip (about few ohms) so that the latter is negligible. As the crack propagates throughout the specimen, it successively cuts the conductive lines, which, each time, makes the global system resistance increase by a constant increment. The time locations of these jumps are detected via an oscilloscope (acquisition rate: 10 MHz) through a voltage divider circuitry. In order to increase the accuracy of jump detection, we used the four channels of the oscilloscope in cascade with different offsets, so that each channel is triggered as the previous one gets out of

its range (Fig. 2a, b). As a result, we obtained the crack length $c(t)$ as a function of time with space and time accuracies of 40 μm and 0.1 μs , respectively (Fig. 2c). The profile of instantaneous velocity $v(c)$ as a function of crack length can then be easily deduced (Fig. 2d).

Finite element analysis was used to estimate the SIF evolution during failure. Figure 3:Top represents the meshing of the complete system. The average mesh size is 1 mm and reduces logarithmically down to 1 nm at the crack tip (Fig. 3:Bottom), in order to resolve in space the crack tip opening. Only half of the system is required for symmetry reasons. Young modulus and Poisson ratio are set to 2.8 GPa and 0.36, respectively (see Table 1). The boundary conditions are the following: (1) The left edge is perfectly adhesive to a polymeric layer of thickness 5 mm, Young's modulus 3 GPa and Poisson ratio 0.41; (2) The left edge of the layer has a no-displacement condition; (3) On the right, the notch is loaded through a L-shaped block, of thickness 5 mm, Young modulus 300 GPa and Poisson ratio 0.4, perfectly adhering to the sample; (4) The L-shaped block is bounded to a virtual roller, the center of which can only move along a line parallel to the wedge side, at a distance equal to the roller radius; (5) The crack edge is stress free; and (6) Vertical displacement is forbidden along the uncracked part of the symmetry plane (top line of Fig. 3:Top). For each sample, the equilibrium position of the wedge yielding the measured applied load at the onset of crack propagation was determined using a plane stress static finite element code (Cast3M 2007). Quasi-static crack propagation is then simulated by increasing the crack length while imposing the wedge position to remain constant. This latter assumption is experimentally justified. Indeed, it has been observed that the load cell signal started to be modified only after a few hundreds of microseconds (typical time of an experiment) after crack initiation¹. This is attributed to the time required

¹ To measure this time shift, we directly connected the Wheatstone bridge of the load cell to an oscilloscope, without passing

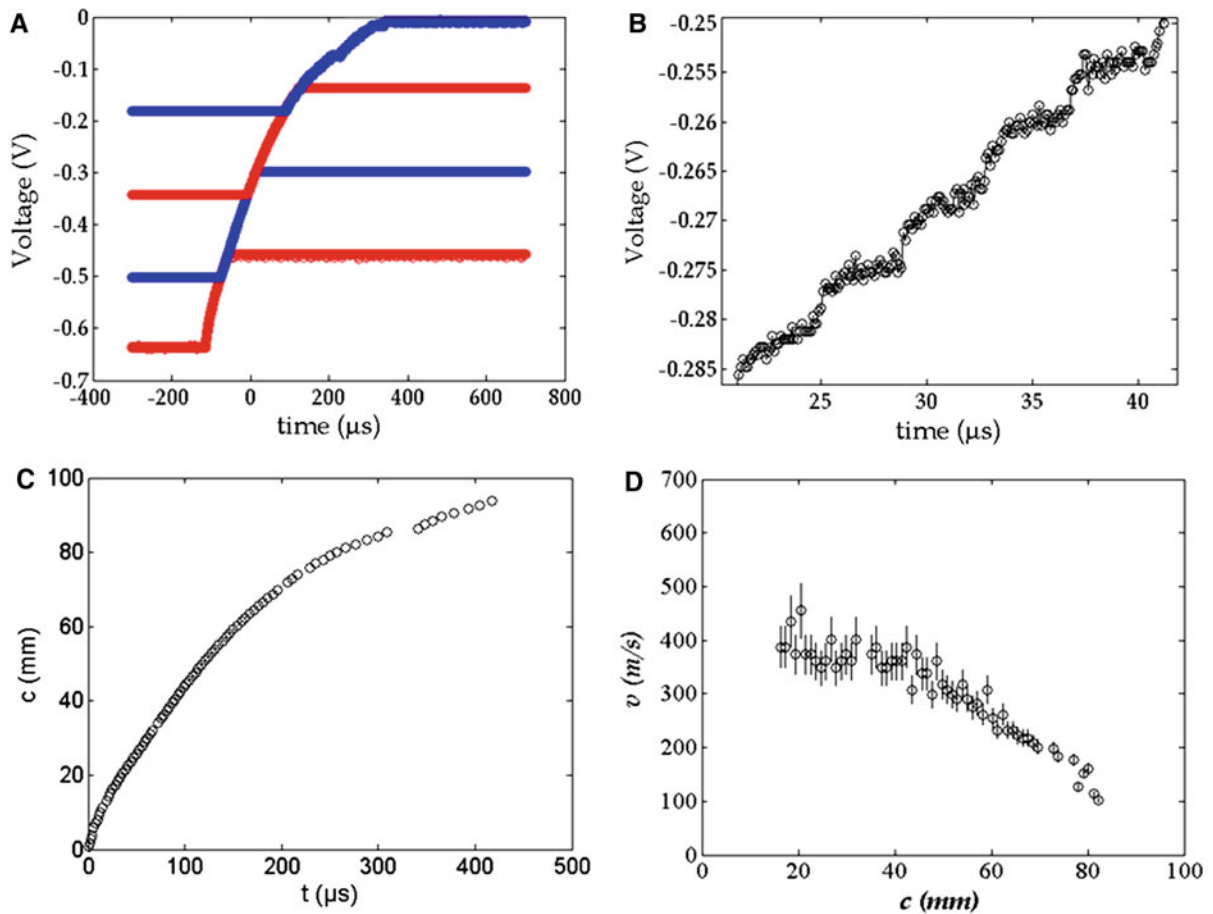


Fig. 2 Measurement of instantaneous crack velocity. **a** Voltage as a function of time as recorded via the oscilloscope. **b** Zoom that permits to distinguish the individual jumps yielded by the

successive cuts of the conductive lines as crack advances. **c** Resulting position of crack tip as a function of time. **d** Final curve showing the variations of crack velocity with crack length

for the sound waves to travel from the crack tip to the load cell. As a result, the wedge position can be assumed to be practically constant during crack propagation. Static SIF is then determined, for each value c of crack length, using the J-integral method (Rice 1968). The validity of our SIF calculation was benchmarked against literature results for wedge-splitting configurations: Our code agreed to better than 2 % with the results of Karihaloo and Xiao (2001) when using their system parameters.

To image the post-mortem fracture surfaces, we used a Leica DM2500 microscope. Most of the images were taken with a $5\times$ objective under polarized light.

The resulting images are $1.4 \times 1 \text{ mm}^2$ in area, with a pixel size of 677 nm. We also imaged the fracture surfaces with an interferometry profilometer (FOGALE Nanotech) which allows one to gather topographical information. These 3D images were taken with a $5\times$ objective. Their area is $1.4 \times 1 \text{ mm}^2$ with a pixel size of $1.86 \mu\text{m}$.

3 Selection of fracture energy with velocity and evidence of a brittle/quasibrittle transition

In each of the experiments performed, both the SIF profile $K(c)$ and the instantaneous velocity profile $v(c)$ have been determined (Fig. 4:Left and center). From these curves, one can derive the profiles of fracture energy, $\Gamma(c)$, using Eq. 1 (Fig. 4:Right). We

Footnote 1 continued through the signal conditioner. This latter, indeed, imposes a time resolution of 1 s.

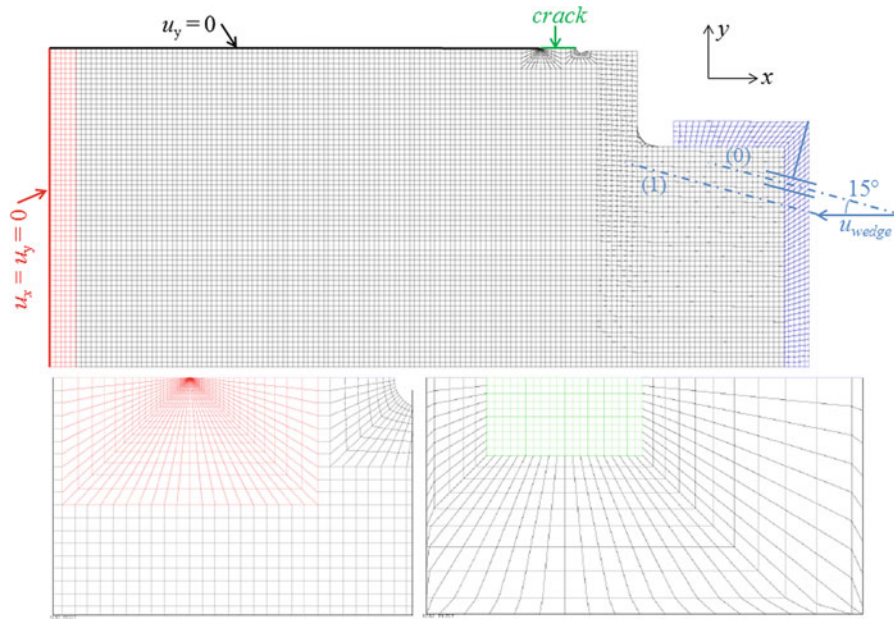


Fig. 3 Computation of SIF. *Top* typical mesh used for finite elements calculations, in order to access the stress/strain fields in the experiments. *Red* polymeric layer. *Black* sample. *Blue* L-shaped block. *Green line* cracked line. The slide link connected to the L-shaped block is used to model the motion of the contact point between the pushed wedge and the roller. Specimen loading is achieved by translating horizontally the slide link, from (0) to

(1), over a distance u_{wedge} selected so that the horizontal force applying on the slide link is half that measured experimentally. *Bottom-Left* zoom on the meshing in the transition region (*red*) between coarse meshing (1 mm mesh size) in the bulk and fine meshing close to the crack tip. On the right is shown part of the circular hole at the seed crack tip. *Bottom-Right* zoom on the crack-tip region (*green*), meshed with a size of 1 nm

note here that Eq. 1 is strictly valid in the case of crack propagation in an elastic half-space, i.e. in the absence of waves emitted by the crack and coming back to it after reflection on sample boundaries (Freund 1990; Goldman et al. 2010). We argue that our experiments are essentially unaffected by such reflected wave for at least two reasons: (1) as measured by Boudet et al. (1995), the sound energy emitted by a crack in PMMA lies within the range 1–4 J/m², a very small value compared to the energy required to fracture the material (a few kJ/m², see below); and (2) this radiated energy is quickly dissipated within the material’s bulk—The acoustic attenuation coefficient has been measured to be 0.67 dB/(cm MHz).

Figure 5 superimposes the various curves Γ versus v measured in the various experiments performed at various levels U_0 of the initially stored mechanical energy. Several regimes can be evidenced:

- For small v , Γ roughly remains constant, close to K_c^2/E , as expected within standard LEFM;
- As v increases and reaches a first critical velocity $v_a \approx 165 \text{ m/s} \approx 0.19C_R$, Γ suddenly increases to

a value about four times larger than $\Gamma(v = 0) = K_c^2/E$;

- Beyond v_a , Γ slowly increases with v ;
- As v reaches a second critical velocity $v_b \approx 350 \text{ m/s} \approx 0.36C_R$, Γ starts to increase rapidly again. It seems to diverge at $v \approx 450 \text{ m/s} \approx 0.5C_R$.

Note also the fairly good collapse of the different curves $\Gamma(v)$ below v_b , and the large dispersion above. This suggests that Eq. 1 is relevant for $v \leq v_b$,—provided a suitable velocity dependence $\Gamma(v)$ is ascribed—, but not beyond. The second critical value $v_b \approx 350 \text{ m/s} \approx 0.36C_R$ is found to correspond to the onset of microbranching instability widely discussed in the literature (see e.g. Fineberg et al. 1992; Sharon and Fineberg 1999). The first critical value $v_a \approx 165 \text{ m/s} \approx 0.19C_R$ was observed in our series of experiments and reported in (Scheibert et al. 2010) for the first time. This observation was made possible by the use of the wedge-splitting geometry, which is a decelerating crack configuration. It offers many data points at relatively low velocities, contrary to most other devices used before. The rapid increase of Γ

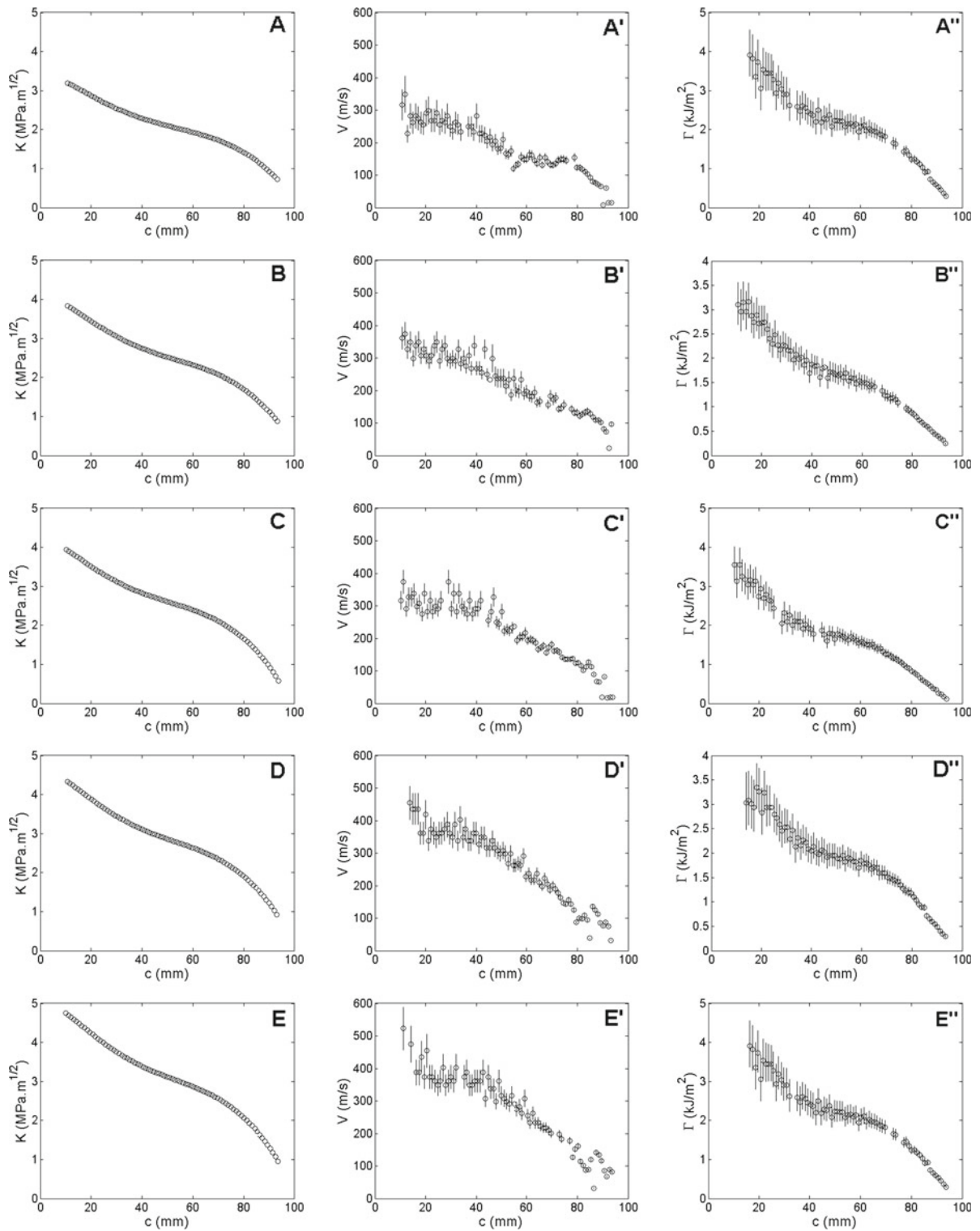


Fig. 4 Variation of SIF K (left), instantaneous crack velocity v (center) and fracture energy Γ (right) as a function of crack length c for five experiments with different stored mechanical

energy U_0 at propagation onset: 2.0 J (A, A' and A''), 2.6 J (B, B' and B''), 2.9 J (C, C' and C''), 3.8 J (D, D' and D''), and 4.2 J (E, E' and E'')

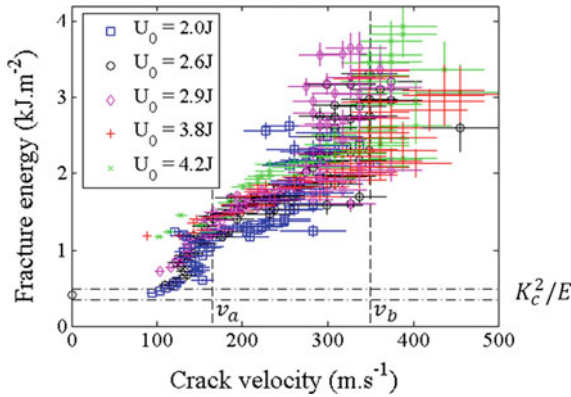


Fig. 5 Fracture energy Γ as a function of crack velocity v for five different experiments with different stored mechanical energies U_0 at crack initiation. The two vertical dashed lines correspond to v_a and v_b . The two horizontal dashed lines indicate the confidence interval (95 %) for the measured fracture energy K_c^2/E at crack initiation (taken from Scheibert et al. (2010))

with v around v_a provides a direct interpretation for the repeated observations of cracks that span a large range of Γ , while keeping a nearly constant velocity about $0.2C_R$ (see e.g. Ravi-Chandar and Knauss 1984; Ravi-Chandar and Yang 1997).

To shed light on the nature of the transition at $v = v_a$ evidenced on the curve relating Γ to v , we examined the post-mortem fracture surfaces and their evolution as crack speed increases (Fig. 6). For v smaller than v_a , fracture surfaces remain smooth at optical scales. But above this threshold, conic marks start to be observed. These marks remain confined within a roughness scale of few micrometers at the fracture surfaces, contrary to the microbranches that deeply develop into the specimen bulk above v_b (see side views and topographical images in Fig. 7).

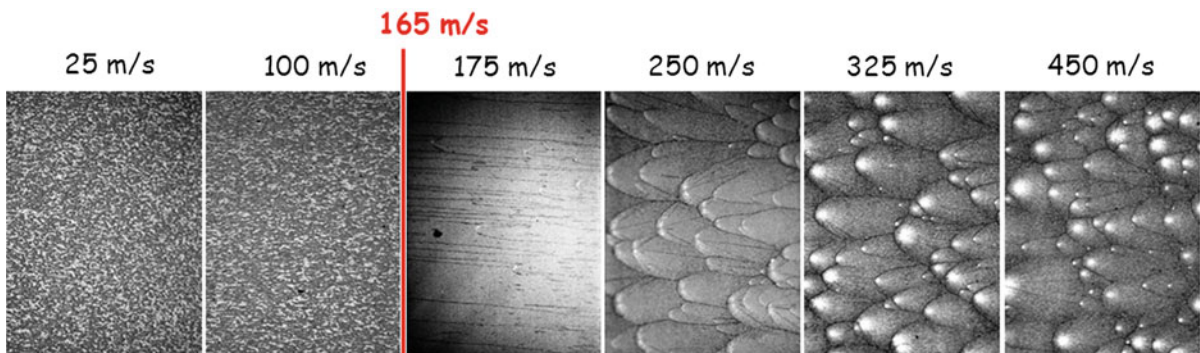


Fig. 6 $1 \times 1.4\text{mm}^2$ microscope images of fracture surfaces created at various speed v

Similar conic marks were reported in the fracture of other brittle materials, among which polystyrene (Regel 1951), oxide glasses (Smekal 1953; Holloway 1968), cellulose acetate (Kies et al. 1950), polycrystalline materials (Irwin and Kies 1952), or homalite (Ravi-Chandar and Yang 1997). They are classically associated (Smekal 1953; Ravi-Chandar and Yang 1997; Rabinovitch et al 2000) with the presence of microcracks that nucleate and grow ahead of the main crack front, and subsequently coalesce with it.

Figure 8 shows the surface density ρ of conic marks as a function of crack speed v . Below v_a , no mark is observed, irrespectively of the chosen magnification (from $5\times$ to $50\times$). Above this value, ρ increases almost linearly with $v - v_a$. The precise correspondence between the critical velocity v_a at which the curve $\Gamma(v)$ exhibits a kink and that at which conic marks start to be observed suggests that both phenomena are the signature of the same transition. Above v_a , PMMA failure switches from nominally brittle to quasi-brittle and goes hand in hand with microcracking that develop ahead of the main front. In the following, we will use the term “Damage Zone” (DZ) to refer to the zone where microcracks develop in the vicinity of the main crack tip. We will distinguish this zone from the FPZ (smaller than the DZ) that embeds dissipative mechanisms (crazing for instance) at the tip of each (micro)crack front.

Note that the region of the fracture surface that bears conic markings also has a characteristic aspect to the naked eye, as it scatters light very efficiently. This is markedly different from the high reflectivity of the region that bears no microcrack. In fractography these regions are classically referred to as the mist and mirror zones, respectively (see e.g. Hull 1999; Rabinovitch

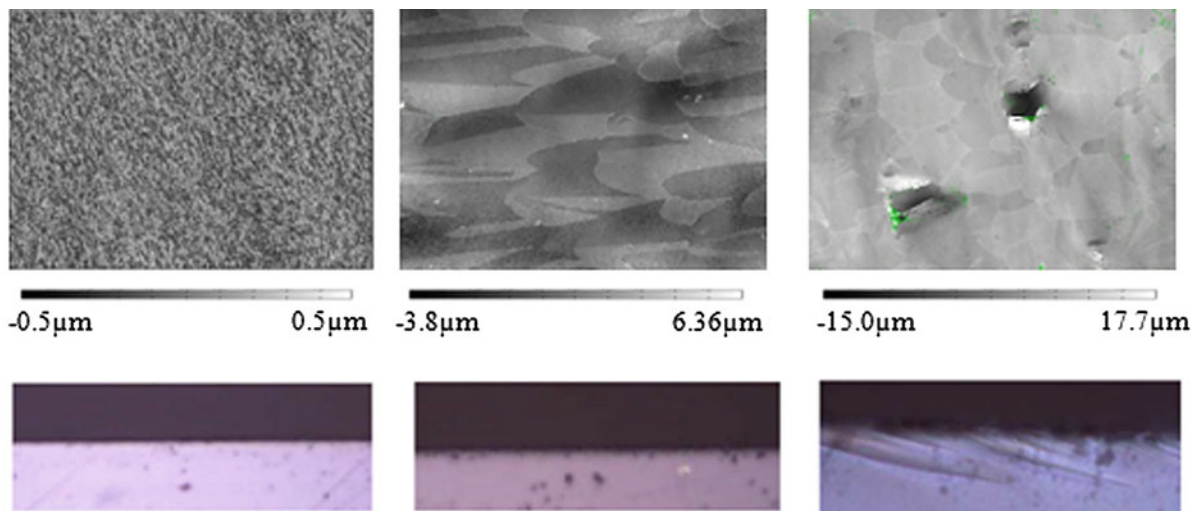


Fig. 7 Profilmetric $1.4 \times 1 \text{ mm}^2$ surface (*Top*) and optical $0.7 \times 0.25 \text{ mm}^2$ side-view (*Bottom*) images taken at velocity smaller than v_a (*left*), between v_a and v_b (*center*), and above v_b (*right*). Crack has propagated from *left* to *right*

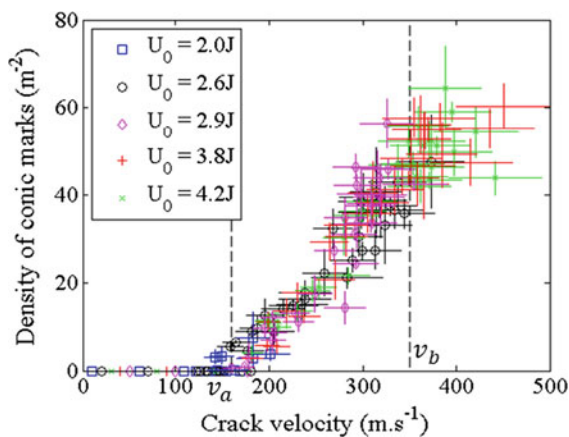


Fig. 8 Surface density ρ of conic marks as a function of crack velocity for five different experiments with different stored mechanical energies U_0 at crack initiation (taken from Scheibert et al. (2010))

and Bahat 2008). Our observation therefore strongly suggests that the mirror/mist transition is simply the morphological counterpart of the brittle/quasi-brittle transition that occurs at v_a

4 Fractographic reconstruction of individual microfailure events

In order to further characterize and understand the dynamics of microcracking events which develop during fast fracture in PMMA ($v > v_a$), we proposed

a numerical reconstruction based on the post-mortem analysis of the traces left by these events (Guerra et al. 2012). The typical time between two successive microcracking events is about 10 ns, which makes them inaccessible using standard techniques as e.g. fast imaging or acoustic emission analysis.

The first step is to identify where microcracks have initiated. On the optical images of post-mortem fracture surfaces (Fig. 9a, b), many well defined points of high optical reflectivity can be seen. These bright/white areas are believed to come from large plastic deformations accompanying the nucleation of microcracks. Thus, they allow us to determine precisely the position of the different nucleation sites. For some microcracks, the precise location of their nucleation site is further constrained by the convergence of fragmentation lines onto it.

The second step is to infer, from the conic patterns, the velocities at which the various microcracks have grown. It is commonly admitted in the literature (Smekal 1953; Ravi-Chandar and Yang 1997; Rabinovitch et al 2000) that the conical marks indicate the intersection points between two interacting microcracks. Let us then consider two microcracks that propagate radially along slightly different planes with velocities c_1 and c_2 (Fig. 9b). The intersection between the initial (micro)crack front and the secondary microcrack leaves a visible trace (i.e. a tiny height difference) on the fracture surfaces. In the coordinate system

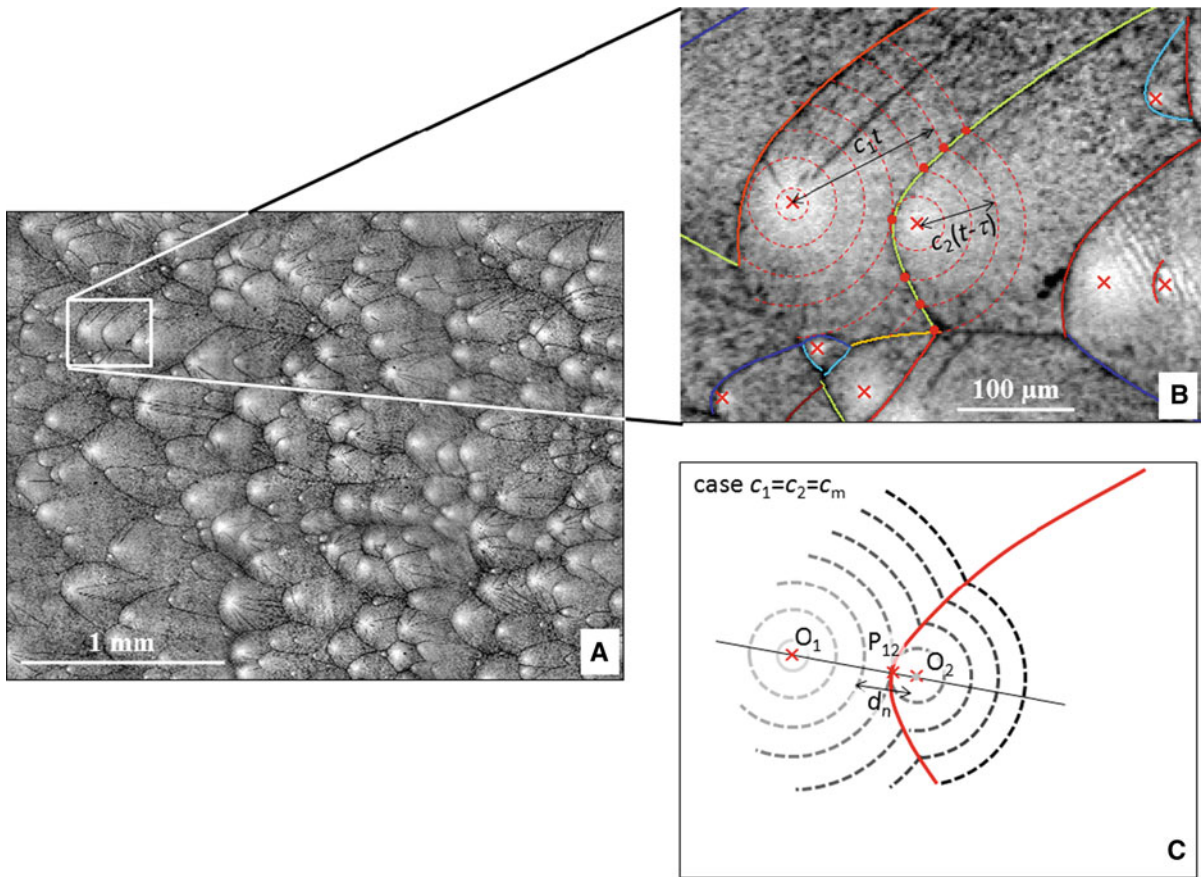


Fig. 9 **a** Typical microscope image of the post-mortem fracture surface. *Bright regions* indicate the nucleation centers. **b** Interpretation of the conic marks: *red dots* sketch the successive positions of the fronts that, by interacting, will be giving rise to the *green branch* of the conic mark. These two microcracks form at $t = 0$ and $t = \tau$, then radially grow at speeds c_1 and c_2 .

Branch fitting via Eq. 2 permits to measure c_2/c_1 . Note that a conic mark can be made of several branches. **c** When $c_2 = c_1$, branches are (mathematical) true conics and the nucleation distance d_n between the front of the incident microcrack (1) and the nucleation point of the forming one (2) is twice the apex-focus distance O_2P_{12} (taken from Guerra et al. (2012))

(e_x, e_y) centered on the site of nucleation of the first microcrack and chosen so that the x -axis passes through the two centers of nucleation, the equation describing the mark left postmortem can be written as (Guerra et al. 2012):

$$\frac{y}{\Delta} = \pm \left[\frac{2c^2}{(c^2-1)^2} \frac{c_1\tau}{\Delta} \sqrt{\left(1 - \frac{2x}{\Delta}\right) (c^2-1) + c^2 \left(\frac{c_1\tau}{\Delta}\right)^2} - \left(\frac{x}{\Delta}\right)^2 + \frac{1}{(c^2-1)^2} + \frac{c^2+1}{(c^2-1)^2} \left(c^2 \left(\frac{c_1\tau}{\Delta}\right)^2 - \frac{2x}{\Delta}\right) \right]^{1/2}, \quad (2)$$

where $c = c_2/c_1$, Δ is the distance between the two nucleation sites, and τ is the time interval between

two microcracking events. The analysis of this equation shows that the number $c_1\tau/\Delta$ sets the aspect ratio of the fractographic trace, while the ratio $c = c_2/c_1$ fixes its form (see Guerra et al. 2012 for details).

We used Eq. 2 to directly extract the ratio $c = c_2/c_1$ for each couple of interacting microcracks (~ 400 couples per image) on different optical pictures obtained at different speeds (Fig. 10). Regardless of the macroscopic crack velocity, we obtain for c a Gaussian distribution centered on 1 with a standard deviation of about 0.03 (Fig. 10). This analysis permits to demonstrate that all microcracks grow at the same velocity c_m inside the DZ. Note that, up to now, nothing prevents c_m to vary with v or K . The mechanism that fixes the value for c_m will be discussed later in this paper (see Sect. 6).

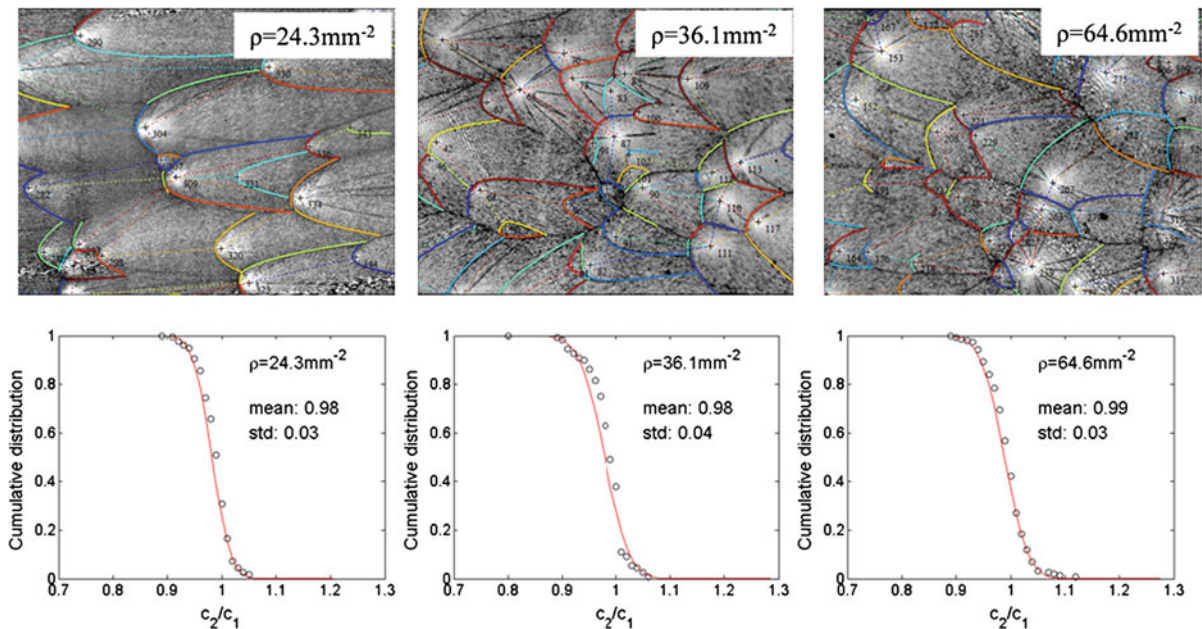


Fig. 10 Direct extraction of the relative speed between two interacting microcracks at three different microcrack densities. (Top) Zones of investigation. Each conic branch has been attributed a given color and the nuclei of the two corresponding interacting microcracks has been joined by a dotted segment of the same color. Note that a conic-like mark is often made of several of these conic branches. The ratio c_2/c_1 is the only adjustable

parameter in Eq. 2 to determine the branch geometry once the nuclei position and the branch apex are set. (Bottom) Corresponding distributions for c_2/c_1 : in the three cases, the distributions are found to fit normal distributions of mean value 0.98–0.99 and standard deviation 0.03–0.04, irrespective of ρ (taken from the supporting information of Guerra et al. (2012))

By using $c_2 = c_1 = c_m$ in Eq. 2, the following relation can be obtained:

$$\frac{y}{\Delta} = \pm \left[4 \frac{d_n(2\Delta - d_n)}{(\Delta - 2d_n)^2} \left(\frac{x}{\Delta}\right)^2 - 4 \frac{d_n(2\Delta - d_n)}{(\Delta - 2d_n)^2} \left(\frac{x}{\Delta}\right) + \frac{d_n(2\Delta - d_n)}{(\Delta - 2d_n)^2} - 4 \frac{d_n}{\Delta} + 4 \left(\frac{d_n}{\Delta}\right)^2 \right]^{1/2}, \quad (3)$$

where $d_n = (\Delta - c_m \tau)$ represents the critical distance between the front of the incident microcrack and the center of the nucleated microcrack at the instant of its nucleation. This distance is twice the distance between the apex and the focus of the considered microcrack and, as such, d_n can be directly extracted from fractographic images (Fig. 9c).

We are now in a position to reconstruct the full dynamics of microcracking events from the knowledge of two series of parameters that can be directly extracted from fractography: The position of nucleation sites and the critical nucleation distance d_n associated to each conic mark. We analyzed several areas of the fracture surfaces, corresponding to various macroscopic

velocities above the microcracking onset ($v > v_a$). In all cases, nine optical images with partial overlap were recorded and gathered into a single large image—This ensures adequate statistics in the following analyses. The methodology to extract the data is the following:

- We record the coordinates x and y of the nucleation sites;
- We estimate the nucleation distance, d_n , by inferring, for each nucleation site, who was the parent microcrack from the relative position of the conics apex with respect to the nucleation site (family criterion). Then, d_n is twice the apex-nucleation center distance.

Following Ravi-Chandar and Yang (1997), the reconstruction is initiated with an originally straight crack front positioned at the left of the zone of analysis. This front propagates from left to right, at a constant velocity of 1 pixel/timestep. Once the distance between one of the microcrack nucleation sites and the primary crack front reaches d_n , a secondary microcrack

starts to grow radially at the same velocity. The front is now the combination of both the translating straight front and the radially growing circular front. Beyond a given time, these two fronts intersect and define the position of the conic mark. When the growing front reaches again a distance d_n associated with another site, a new microcrack is nucleated. The procedure is repeated until all the nucleation sites have been triggered.

Figure 11 shows two examples of reconstruction for two different macroscopic velocities and Fig. 12 superimposes the conic marks obtained by the simulation to those really observed in fractography. We note the fairly good agreement between experiment and reconstruction away from the edges (in the center of the images). This permits to validate the method. Thanks to it, we are able to reconstruct deterministically the dynamics of micro-damage during fast fracture in PMMA from the observation and analysis of the patterns observed on the post-mortem fracture surfaces. We emphasize the resulting resolution of $\sim 1 \mu\text{m}$ (1 pixel) in space, and of 10 ns in time (pixel size/ c_m with $c_m \approx 200 \text{ m/s}$ as it will be demonstrated further in the paper). This is far better than what can be obtained via conventional experimental mechanics methods as e.g. acoustic emission or fast imaging methods.

Note however some discrepancies between experiments and reconstructions on the left, top and bottom edges of the analyzed zones. Such finite size problems are unavoidable. Along the top and bottom sides of the image, the influence of microcracks outside the field of view are naturally ignored. Also, a non-realistic straight vertical front has been used, as we cannot predict the precise instants at which the leftmost centers have turned to microcracks during the reconstruction. In order to test the sensitivity of the reconstruction to the initial front shape, we have performed different simulations with the same inputs except the initial front shape. In Fig. 13, three different cases are tested: (1) a straight vertical front, (2) a sinusoidal front with an amplitude and a period equivalent to the mean value of a wavy front far from the first step in previous reconstruction and (3) the same sinusoidal front vertically shifted by half a period. We can observe that, except of course at the very beginning of the simulation (i.e. on left side of the images), the difference between these three cases are very small. Moreover, these small differences tend to disappear as the front to propagate, i.e. as more and more microcracks are

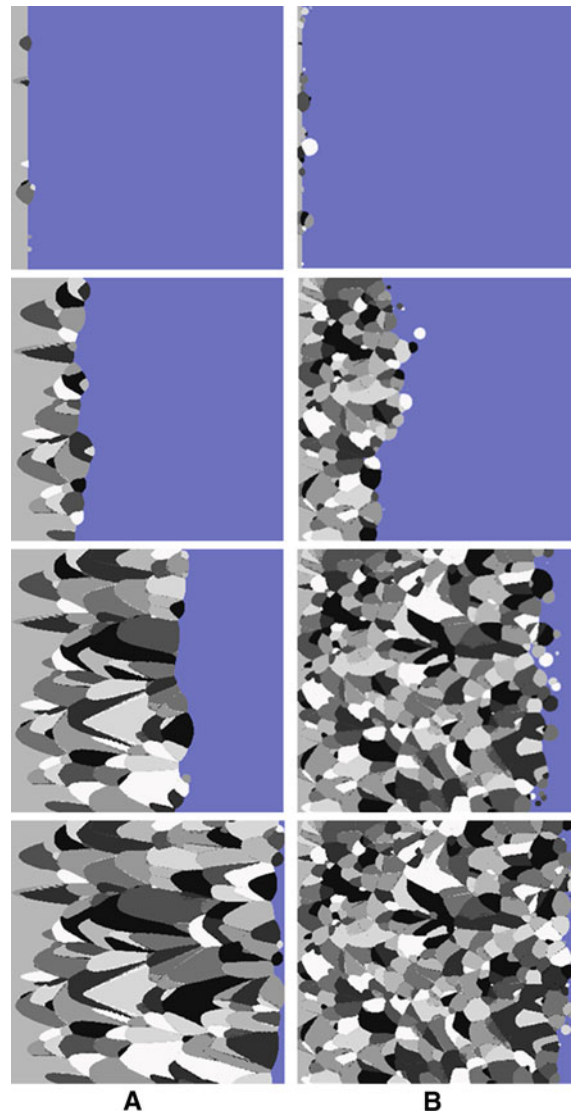


Fig. 11 Reconstructed sequence of crack propagation and microfailure events at the microscale for two different values of K , namely $K = 2.53 \text{ MPa } \sqrt{\text{m}}$ (left) and $K = 4.18 \text{ MPa } \sqrt{\text{m}}$ (right). The blue part corresponds to uncracked material and we ascribed an arbitrary gray level to each of the growing microcrack. From this, one can deduce the intersection points between microcracks that coincide with the observed conics marks on the fracture surfaces. The size of the two zones of analysis is $2.5 \times 2.5 \text{ mm}^2$. The macroscopic crack propagates from left to right

involved. In some cases, we have observed differences propagating over the whole image. Perfect reconstructions would be reached only by analyzing the whole fracture surfaces, and not some partial areas. Knowing all the history of crack propagation is the only

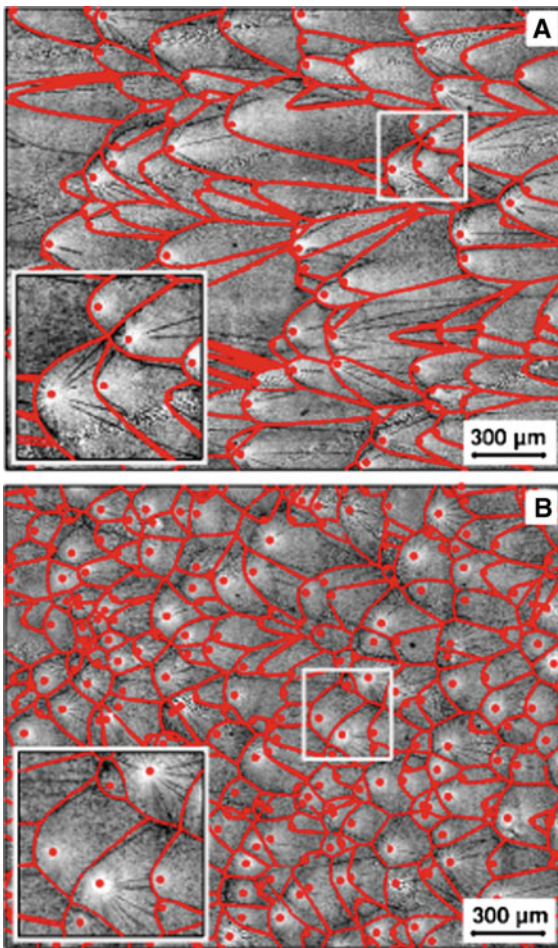


Fig. 12 Qualification of the procedure: superimposition of the conic pattern as obtained from reconstruction onto that observed by fractography. **a** $K = 2.77 \text{ MPa} \sqrt{\text{m}}$. **b** $K = 4.18 \text{ MPa} \sqrt{\text{m}}$. *Red dots* indicate nucleation centers (taken from the supporting information of Guerra et al. (2012))

solution for the determination of the real initial front shape which could allow a perfect reconstruction.

5 Quantitative selection of the microdamaging state by crack loading

The reconstruction method, described in the previous section, shows that the dynamics of micro-damage is entirely determined by the position of nucleation sites, the nucleation distances d_n , and the microscopic velocity of the fronts c_m . To understand what selects these three parameters, they will be explored in more detail.

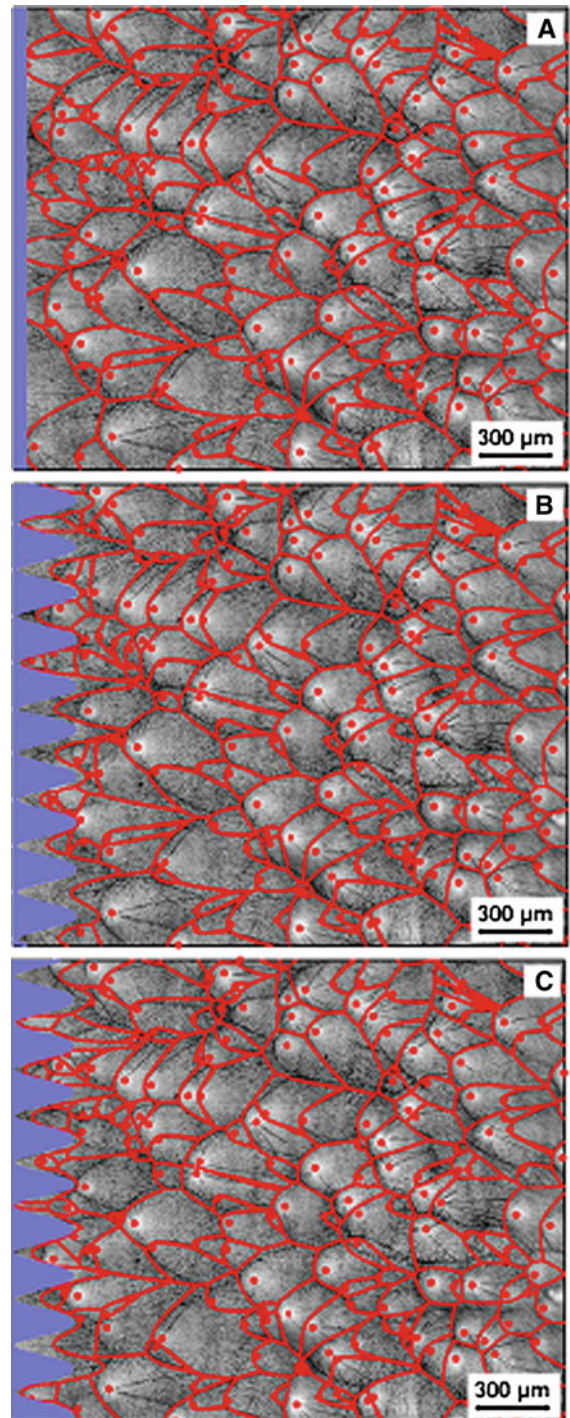


Fig. 13 Influence of initial crack front morphology on the reconstruction for $\rho = 45.0 \text{ mm}^{-2}$ ($K = 3.65 \text{ MPa} \sqrt{\text{m}}$). Three different initial conditions were used. **a** *Straight vertical line*. **b** *Vertical sinusoidal shape* with a period of $186 \mu\text{m}$ and a peak-to-peak amplitude of $242 \mu\text{m}$. **c** *Same sinusoidal shape*, but translated vertically over half a period (taken from the supplementary information of Guerra et al. (2012))

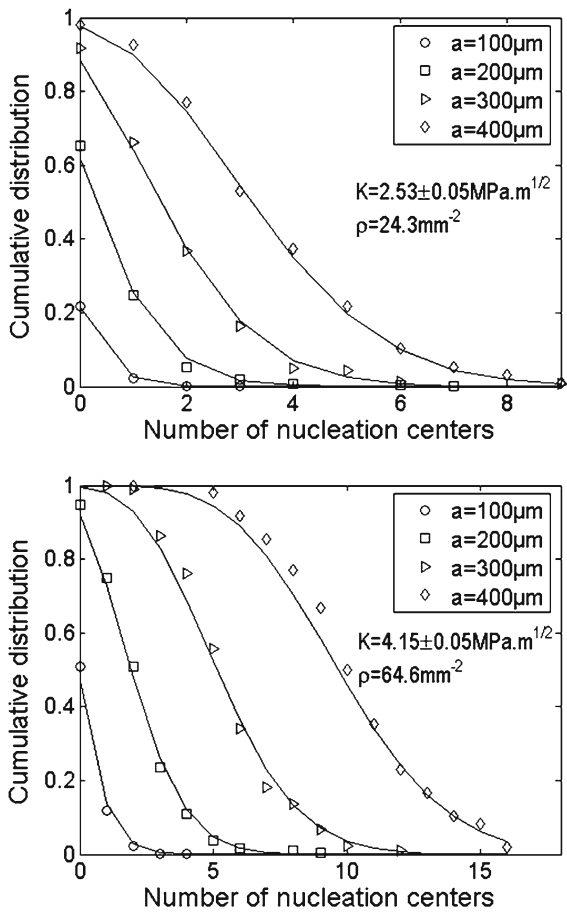


Fig. 14 Cumulative distribution of the number of nucleation centers contained in square regions of lateral size a , for two different fractographic images. *Solid lines* represent Poisson fits of parameter ρa^2 , where the fitted value ρ can be identified with the center density

5.1 Spatial distribution of nucleation centers

To characterize the spatial distribution of nucleation sites, we computed the distribution of the number of sites that can be observed on a square of a given size a . Figure 14 shows these distributions for two different fractographic pictures, i.e. for two values of K . These distributions follow a Poisson distribution with a single parameter ρa^2 where ρ is constant over a given fractographic picture but varies with K . This reflects a homogeneous and uncorrelated distribution of the sites all along the post-mortem fracture surface. Then, ρ can be identified with the surface density of nucleation sites and fully characterizes their spatial distribution.

Figure 15 presents the evolution of ρ with loading K . The density is naturally zero for K smaller

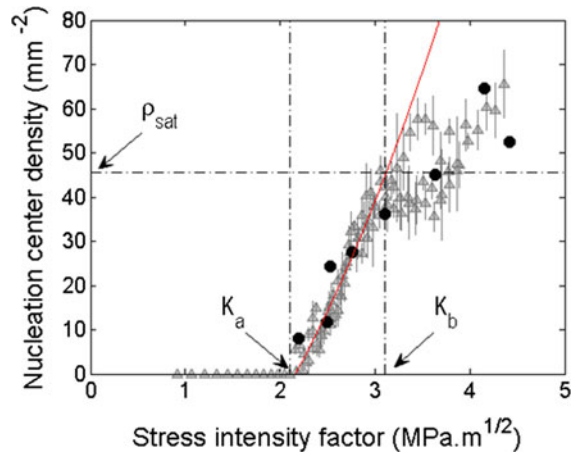


Fig. 15 Variation of the density ρ of nucleation centers with applied SIF. *Black disks* correspond to the eight images on which post-mortem reconstruction was performed. *Red line* is a fit via Eq. 4. K_a and K_b are associated with microcracking and microbranching onset, respectively (taken from Guerra et al. (2012))

than K_a (SIF value at microcracking onset, i.e. when $v = v_a$) as there is no microcracking. Beyond this value, it increases with K . Also, this curve exhibits large fluctuations and seems to saturate when the density reaches a value $\rho_{sat} \approx 45.5 \text{ mm}^2$, beyond K_b . Note that this latter value coincide with microbranching onset and, therefore the $\rho(K)$ curve does not really make sense above K_b since the front has splitted into various microbranches, which prevents us from correlating the macroscopic K value to the number of conic marks on the main crack only.

To account for the curve $\rho(K)$, let us consider (Scheibert et al. 2010) that a discrete population of weak localized zones is present within the material with a bulk density ρ_v . Let us then assume that a microcrack can nucleate in these areas provided the two following conditions are fulfilled:

- The local stress at the considered zone is large enough, i.e. larger than a given threshold value σ^* (smaller than the yield limit σ_Y of the material);
- The considered zone is far enough from the main crack front to allow the microcrack to grow, i.e. at a distance greater than d_a .

The density ρ of nucleated microcracks per unit area of fracture is then given by $\rho_v \{h_{\perp} - d_a\}$ where h_{\perp} is the thickness of the layer where the stress has exceeded σ^* (h_{\perp} is measured perpendicular to the mean plane of fracture). The singular form of the stress field at crack tip leads to write $h_{\perp} \propto K^2/\sigma^{*2}$, which yields

(Scheibert et al. 2010):

$$\begin{aligned} \rho &= 0 && \text{for } K \leq K_a \\ \rho &\propto K^2 - K_a^2 && \text{for } K \geq K_a, \end{aligned} \quad (4)$$

with $K_a \propto \sigma^* \sqrt{d_a}$. This equation, plotted in red on Fig. 15, reproduced quite well the experimental data below K_b .

As the determination of ρ from fracture surface is much more accurate and consensual than the determination of K (based on FEM calculation with inherent approximations), in the following, we will use ρ rather than K as the control parameter as a function of which the various quantities further defined in this paper will be plotted. Indeed, ρ fully characterizes the spatial distribution of nucleation sites and monotonically evolves with K within the relevant range $K_a \leq K \leq K_b$.

5.2 Chronology of microfailure events

Figure 16 shows the cumulative distribution of nucleation distances d_n measured on two typical fracture surfaces. The probability density function (derived from the cumulative distribution) is zero for $d_n \leq d_{\min}$, maximum at d_{\min} , subsequently linearly decreases, and is finally zero as d_n exceeds d_{\max} . This distribution form was observed for all the fracture surfaces, irrespectively of ρ . d_{\max} is found to increase with ρ , while d_{\min} decreases with ρ and remains very close to zero (Guerra et al. 2012).

The variation of the mean value \bar{d}_n of d_n with ρ exhibits two regimes (Fig. 17:Top): (1) A linear increase with ρ followed by (2) a saturation ($\bar{d}_n^{\text{sat}} \approx 50 \mu\text{m}$) when ρ is greater than the value ρ_{sat} associated in Fig. 15 with the microbranching onset (at $K = K_b$).

To understand the saturation origin, we plotted, on Fig. 17:Bottom, the evolution of the mean nearest-neighbor distance $\langle \Delta r \rangle$ with ρ as it is predicted for a 2D Poissonian spatial distribution ($\langle \Delta r \rangle = 1/(2\sqrt{\rho})$). The plotted errorbars also indicate the associated standard deviation ($\sigma_{\Delta r} = \sqrt{(4-\pi)/(4\pi\rho)}$). When ρ reaches ρ_{sat} , in some cases, the distance between two neighbouring nucleation centers is of the order of the nucleation distance. As a result, two centers can nucleate almost at the same time (avalanche effect). The number of microcracks involved in such avalanches, also plotted in the figure, increases in the vicinity of ρ_{sat} . This strongly suggests that the observed saturation in the d_n evolution (Fig. 17:Top) results from this steric effect.

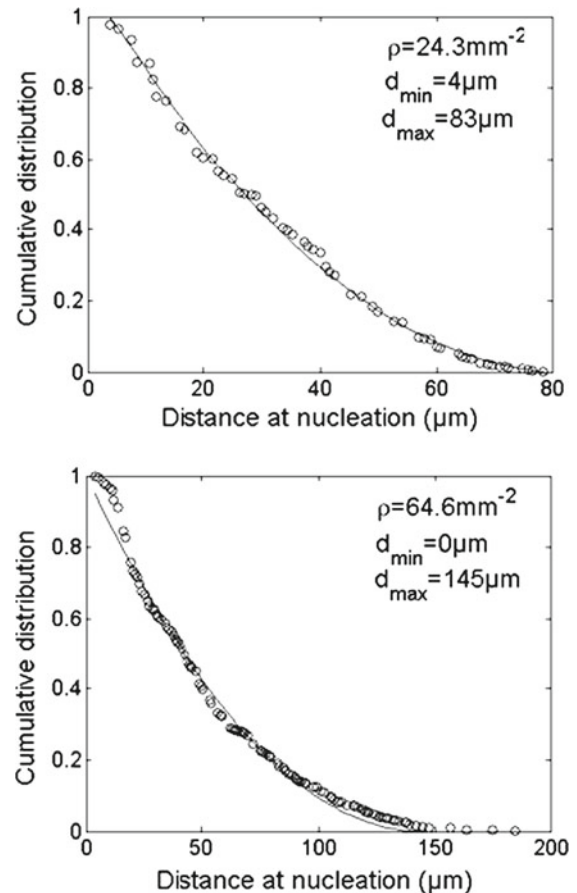


Fig. 16 Cumulative distribution of the nucleation distances d_n , as measured for two different fractographic images. *Solid lines* are fits with $P(d_n) = ((d_{\max} - d_n)/(d_{\max} - d_{\min}))^2$

5.3 Velocity of microcrack growth

The fractographic analysis performed in Sect. 4 showed that, within the DZ, all microcracks grow at the same velocity c_m . Unfortunately, it does not allow us to directly measure the value of c_m and its possible dependence with ρ . Indeed, Eq. 2 shows that the form taken by the conical bands depends only on the position of the nucleation sites and on the nucleation distance but not on the value of c_m .

We propose to use the deterministic reconstructions obtained in Sect. 4 to connect the macroscopic crack speed v to c_m . Figure 18a shows the evolution of the mean front position measured from reconstructions of different fracture surfaces (i.e. for different densities of nucleation centers) as a function of numerical time step normalized by c_m (homogeneous to a distance,

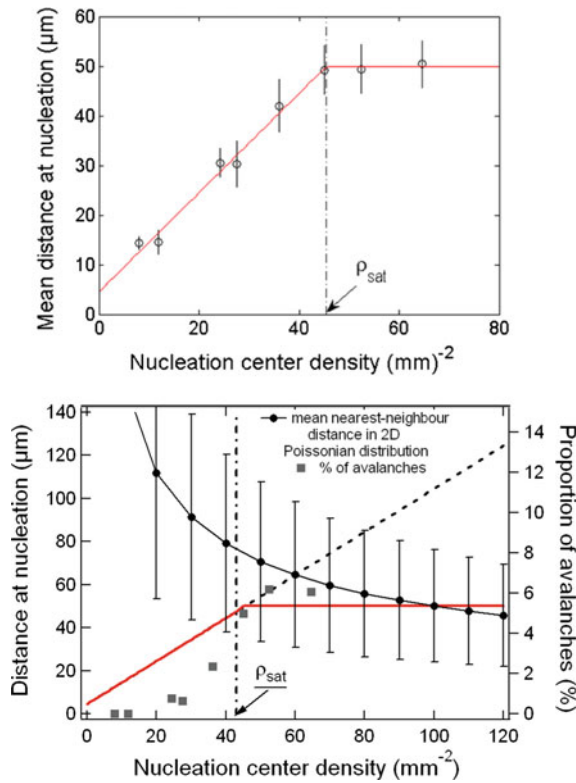


Fig. 17 *Top* mean distance at nucleation \bar{d}_n as a function of ρ . The red curve is a linear fit over $\rho \leq \rho_{sat} = 45.5 \text{ mm}^{-2}$ and a plateau at $\bar{d}_n^{sat} = 50 \mu\text{m}$ over ρ_{sat} . *Bottom* saturation of \bar{d}_n and avalanches. The red line is the same as in the top figure. It is compared to the mean nearest-neighbor distance in a Poissonian distribution (black solid line). Solid squares indicate the proportion of microcracks involved in avalanches, as computed from the reconstruction

corresponding to the distance travelled by a crack front at a velocity c_m in absence of microcracking events). All the curves are linear with a slope A that defines the ratio v/c_m . At this point, one should recall that the reconstruction procedure starts with an unrealistic initial straight crack front. We checked that this does not affect the measured value A (Guerra et al. 2012). Then, since v is known, c_m can be deduced and plotted, on Fig. 18b as a function of ρ . This microscopic velocity is found to be a constant, $c_m \approx 217 \text{ m/s} = 0.24c_R$, independent of the loading K , the density ρ , and the macroscale velocity v . The implications of this result will be further discussed in the next section.

The fracture energy measurements $\Gamma(v)$ made in Sect. 3 will now allow us to understand why such a constant velocity c_m is selected within the microcracking regime. Figure 19 shows the evolution of Γ with

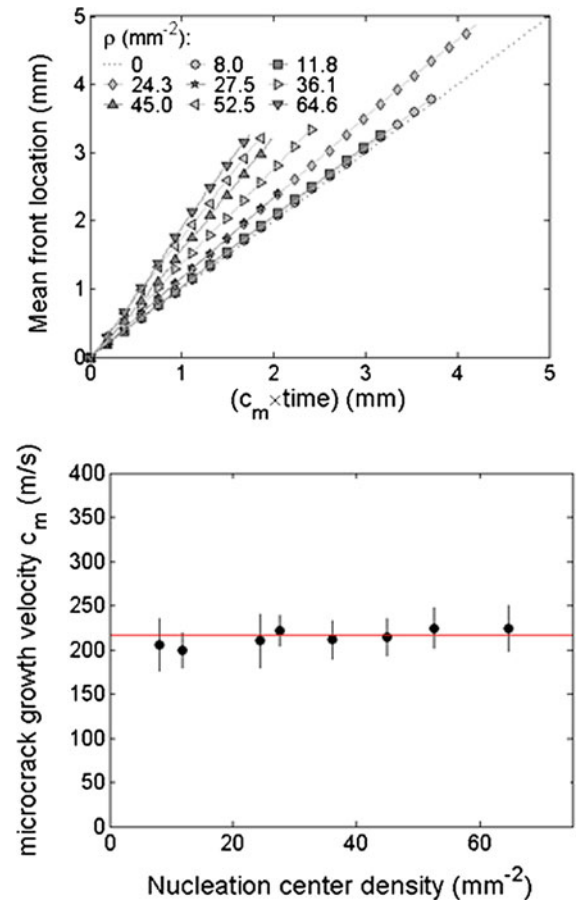


Fig. 18 Determination of the local propagation velocity c_m of individual microcracks. *Left* evolution of the mean crack front position as a function of $c_m \times t$. Different curves correspond to different fractographic images with different microcrack density. Slope of these curves defines the ratio A between continuum-level scale failure velocity v and microcrack velocity c_m . *Right* variation of c_m with ρ . Horizontal red line indicates the mean value $c_m \approx 217 \text{ m/s}$

the dynamic SIF K_d . In the low speed regime (i.e. for low K_d) where crack propagates without involving any microdamaging or microbranching, Γ scales with K_d^2 . We can also expect that the FPZ size R_c scales with K_d^2 : $R_c = K_d^2/\alpha\sigma_Y^2$ where α is a constant of order 1, and σ_Y is the material's yield stress. The scaling of Γ with K_d thus indicates a linear variation between Γ and R_c and, following Scheibert et al. (2010), a constant dissipated energy ϵ per volume unit within the FPZ. The fracture energy then writes:

$$\Gamma = \frac{\epsilon}{\alpha\sigma_Y^2} K_d^2 + \left(\frac{1}{E} - \frac{\epsilon}{\alpha\sigma_Y^2} \right) K_c^2 \tag{5}$$

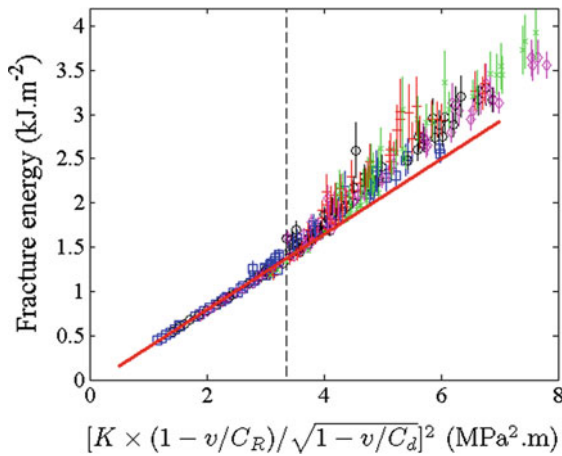


Fig. 19 Variation of the fracture energy Γ with $K_d = K \times (1 - v/C_R)/\sqrt{1 - v/C_D}$. The vertical dashed line corresponds to microcracking onset $K_d^q = 1.83 \text{ MPa} \sqrt{\text{m}}$. Note that K_d can *stricto-sensu* be identified with the dynamic SIF in absence of microcracking, i.e. for $K_d \leq K_d^q$. The solid red line is a fit with Eq. 5

As long as $v \leq v_a$ (thus without microdamage), one can relate K_d to K (Freund 1990): $K_d = K \times (1 - v/C_R)/\sqrt{1 - v/C_D}$ where C_D refers to the speed of dilational waves (cf. Table 1). By replacing K with K_d in Eq. 1, and by subsequently injecting the result in Eq. 5, one gets the following expression for Γ versus v :

$$\Gamma = \frac{1 - \frac{\epsilon E}{\alpha \sigma_Y^2}}{1 - \frac{\epsilon E}{\alpha \sigma_Y^2} \frac{1-v/C_R}{1-v/C_D}} \frac{K_c^2}{E} \quad (6)$$

This expression yields a divergence of Γ at a finite velocity c_∞ given by:

$$c_\infty = \left(\frac{\epsilon E}{\alpha \sigma_Y^2} - 1 \right) \frac{C_R C_D}{\frac{\epsilon E}{\alpha \sigma_Y^2} C_D - C_R} \quad (7)$$

In this expression, the only unknown quantity is $\epsilon/\alpha \sigma_Y^2$. This can be evaluated by fitting the first linear part (i.e for $K_d \leq K_d^q$) of the curve Γ versus K_d^2/E plotted in Fig. 19 with Eq. 5. One then gets:

$$c_\infty \simeq 204 \text{ m/s} = 0.23 C_R \quad (8)$$

This value sets the maximum crack growth velocity in the absence of microcracking: Beyond c_∞ dissipation diverges within the FPZ. Assuming that the same dissipation mechanisms are involved within the FPZ of each microcrack when $v > v_a$, we expect that the limiting speed of microcracks is also determined by c_∞ , so that $c_m \approx c_\infty$.

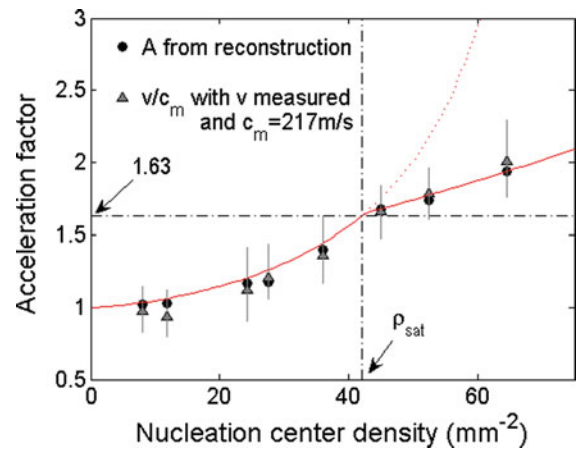


Fig. 20 Acceleration factor $A = v/c_m$ as a function of the microcrack density ρ . Red line is a fit by Eq. 9 with $b = 1.19 \pm 0.02$. Horizontal dot line defines v_b/c_m and passes through the slope breakdown observed when $\rho = \rho_{sat}$ (taken from Guerra et al. (2012))

6 Role of microdamaging in the selection of continuum-level scale failure velocity

The previous section has allowed us to better understand how the different variables that characterize the microdamage developing within the DZ are selected when v exceeds v_a . The most surprising observation concerns the propagation velocity of microcracks c_m that remains constant, of the order of 217 m/s, and significantly lower than the macroscopic velocity v . In other terms, damage does not slow down the macroscopic crack tip as it was commonly believed until now (Ravi-Chandar 2004; Ravi-Chandar and Yang 1997; Washbaugh and Knauss 1994), but on the contrary it accelerates it. And this acceleration factor is all the more important as ρ (or equivalently K) increases (Fig. 20).

The temporal evolution of a given point on the main front, shown in Fig. 21, permits to better understand the effect of microdamage on the dynamics of macroscopic cracking. The trajectory of this point exhibits random and sudden jumps. These jumps actually correspond to the coalescence of a microcrack with the main front. Between these events, the local front velocity remains close to c_m (i.e. the slope is equal to 1). Such an acceleration effect can be captured by a simple mean-field model, detailed in Guerra et al. (2012), which simply consists in counting the number of coalescence events as the main front propagates over a unit of length when

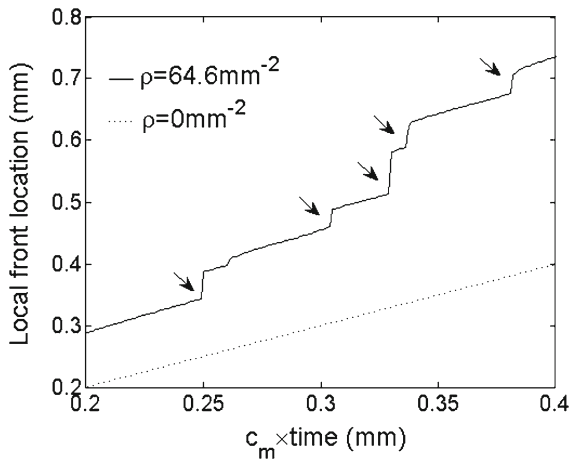


Fig. 21 Position of a given point of the front as a function of “time” $c_m \times t$ as obtained from the reconstructed simulation, applied to a fracture surface with $\rho = 64.6 \text{ mm}^{-2}$. The dotted straight line indicates the expected position without microdamage (slope 1). The jumps (arrows) correspond to coalescence events with microcracks (taken from Guerra et al. (2012))

the nucleation sites are located at the nodes of a square lattice. One then gets:

$$A = \frac{1}{1 - b\bar{d}_n\sqrt{\rho}} \tag{9}$$

where b is a numerical factor close to 1. This equation, combined with the evolution of \bar{d}_n with ρ (red line in Fig. 17:Top) is plotted in red in Fig. 20. It reproduces quite well both the data coming from experiments (grey triangles) and from the reconstruction (black circle). Note the change in slope observed at ρ_{sat} . At this point, $A = A_b = 1.63$. This corresponds to a ratio $A_b \simeq v_b/c_m$ where $v_b \simeq 0.4C_R$ is associated with the microbranching onset. This strongly suggests that the steric effect at the origin of the saturation of d_n also plays a role (still unsolved) in the micro-branching instability.

7 Conclusion

The series of experiments reported here were designed to shed light on the dissipation mechanisms that develop during fast crack growth in PMMA. They reveal that, above a well-defined critical velocity, PMMA stops to behave *stricto sensu* as a nominally brittle material and crack propagation goes hand in hand with microcracks that nucleate and grow ahead of the main front. Those let characteristic marks (referred

to as conic marks) on post-mortem fracture surfaces, the morphological analysis of which allowed us to reconstruct the full dynamics of microfailure events. The simultaneous space and time accuracies were of the order of the micrometer and the tens on nanoseconds, *i.e.* far better than what was reachable up to now.

Analysis of the reconstructions demonstrated that the true local propagation velocity of single cracks remains limited to a fairly low value $c_m \simeq 0.23c_R$ in PMMA, while the *apparent* fracture velocity measured at the continuum-level scale (*e.g.* via potential drop method) can be much higher (up to twice larger!). Such an anomalously high measured velocity results in fact from the coalescence of microcracks with each other and with the main front—all of them growing at c_m . In other words, the main effect of microdamaging is not, as commonly believed up to now (Washabaugh and Knauss 1994; Ravi-Chandar 2004; Ravi-Chandar and Yang 1997), to slow down fracture by increasing dissipation within the DZ, but on the contrary to boost the propagation of the main crack.

The value c_m that limits the true local velocity of single crack fronts in PMMA in the dynamic regime is set by the physico-chemical dissipative and non-linear processes that develop within the FPZ, *e.g.* thermal (Estevez et al. 2000), viscoelastic effects (Boudet et al. 1996; Persson and Brener 2005) or hyperelastic processes (Bouchbinder et al. 2008; Livne et al. 2010; Buehler et al. 2003). Hence, it will depend on the considered material. On the other hand, the boost effect induced by microdamaging takes the form of a purely geometrical factor controlled by two quantities: the density ρ of nucleation sites and the mean distance \bar{d}_n at nucleation. These two variables fully characterize the damaging state within DZ and evolve with K . Once ascribed, they permit to relate the continuum-level fracture speed v to the true local propagation speed c_m . Further work is required to unravel how PMMA internal structure selects the material-dependent quantities c_m , $\rho(K)$, and \bar{d}_n .

The presence of microcracks forming ahead of a dynamically growing crack has been evidenced in a variety of materials, *e.g.* in most brittle polymers (Ravi-Chandar 1998; Du et al. 2010), in rocks (Ahrens and Rubin 1993), in some nanophase ceramics and nanocomposites (Rountree et al. 2002), in oxide glasses (Rountree et al 2010), in metallic glasses (Murali et al. 2011), etc. The boost mechanism demonstrated here on PMMA is expected to hold in this whole class of

materials. Note that a similar effect has also been invoked (Prades et al 2005) in oxide glasses under stress corrosion, where ultra-slow crack propagation (down to few tenths of nanometers per second) was found to involve "nano"-cracks forming ahead of the main crack tip (Célerié et al. 2003; Celarié et al. 2003; Bonamy et al. 2006; Ferretti et al. 2011). This yields us to conjecture that failures with anomalously high apparent velocities measured at continuum-level scale may arise in all situations involving propagation-triggered microcracks, including *e.g.* shear fracture in compressed granite (Moore and Lockner 1995), thermal failure in shale (Kobchenko et al. 2011; Panahi et al. 2012), and more generally failure of so-called quasi-brittle materials. One of the most robust observations in this field is the power-law form followed by the distribution in size and in time interval between two successive microfailure events (see Bonamy 2009; Deschanel et al. 2009 for recent reviews). It would be interesting to see whether or not the microcracking evidenced here in dynamic failure regime share the same scale-free features and how this affects the boost effect. Work in this direction is under way.

Acknowledgments We warmly thank K. Ravi-Chandar (Univ. of Texas, Austin) for many illuminating discussions. We also thank T. Bernard (SPCSI) for technical support, P. Viel and M. Laurent (SPCSI) for gold deposits, and A. Prevost (ENS, Paris) for his help with the profilometry measurements at ENS. We also acknowledge funding from French ANR through Grant No. ANR-05-JCJC-0088 and from Triangle de la Physique through Grant No. 2007-46.

References

- Adda-Bedia M, Arias R, Ben-Amar M, Lund F (1999) Dynamic instability of brittle fracture. *Phys Rev Lett* 82:2314
- Ahrens TJ, Rubin AM (1993) Impact-induced tensional failure in rocks. *J Geophys Res Planets* 98:1185
- Anthony SR, Chub JP, Congleton J (1970) The crack branching velocity. *Philos Mag* 22:1201
- Bergkvist H (1974) Some experiments on crack motion and arrest in polymethylmethacrylate. *Eng Fract Mech* 6:621
- Bonamy D (2009) Intermittency and roughening in the failure of brittle heterogeneous materials. *J Phys D Appl Phys* 42:214014
- Bonamy D, Prades S, Rountree CL, Ponson L, Dalmas D, Bouchaud E, Ravi-Chandar K, Guillot C (2006) Nanoscale damage during fracture in silica glass. *Int J Fract* 140:3
- Bouchbinder E, Mathiesen J, Procaccia I (2005) Branching instabilities in rapid fracture: dynamics and geometry. *Phys Rev E* 71:056118
- Bouchbinder E, Livne A, Fineberg J (2008) Weakly nonlinear theory of dynamic fracture. *Phys Rev Lett* 101:264302
- Bouchbinder E, Marder M, Fineberg J (2010) The physics of simple cracks. *Annu Rev Condens Matter Phys* 1:371
- Boudet JF, Ciliberto S, Steinberg V (1995) Experimental study of the instability of crack propagation in brittle materials. *Europhys Lett* 30:337
- Boudet JF, Ciliberto S, Steinberg V (1996) Dynamics of crack propagation in brittle materials. *J Phys II Fr* 6:1493
- Bruhwieler E, Wittmann FH (1990) The wedge splitting test: a method for performing stable fracture mechanics tests. *Eng Fract Mech* 35:117
- Buehler MJ, Abraham FF, Gao HJ (2003) Hyperelasticity governs dynamic fracture at a critical length scale. *Nature* 426:141
- Cast3M finite element code: <http://www-Cast3M.cea.fr/>
- Celarié F, Prades S, Bonamy D, Dickel A, Bouchaud E, Guillot C, Marlière C (2003) Surface fracture of glassy materials as detected by real-time atomic force microscopy (afm) experiments. *Appl Surf Sci* 212:92–96
- Célerié F, Prades S, Bonamy D, Ferrero L, Bouchaud E, Guillot C, Marlière C (2003) Glass breaks like metal but at the nanometer scale. *Phys Rev Lett* 90:075504
- Cotterell B (1968) Fracture propagation in organic glasses. *Int J Fract* 4:209
- Deschanel S, Vanel L, Godin N, Maire E, Vigier G, Ciliberto S (2009) Mechanical response and fracture dynamics of polymeric foams. *J Phys D Appl Phys* 42:214001
- Du P, Xue B, Song Y, Zuo M, Lu S, Zheng Q, Yu J (2010) Experimental observation and computer simulation of conic markings on fracture surfaces of polymers. *J Mater Sci* 45:3088
- Estevez R, Tijssens MGA, der Giessen EV (2000) Modeling of the competition between shear yielding and crazing brittle polymers. *J Mech Phys Solids* 48:2585
- Ferretti D, Rossi M, Royer-Carfagni G (2011) An espi experimental study on the phenomenon of fracture in glass. Is it brittle or plastic? *J Mech Phys Solids* 59:1338–1354
- Fineberg J, Gross SP, Marder M, Swinney HL (1992) Instability in the propagation of fast cracks. *Phys Rev B* 45:5146
- Fond C, Schirrer R (2001) Dynamic fracture surface energy values and branching instabilities during rapid crack propagation in rubber toughened pmma. *C R Acad Sci Paris* 329:195
- Freund LB (1990) *Dynamic fracture mechanics*. Cambridge University Press, Cambridge
- Goldman T, Livne A, Fineberg J (2010) Acquisition of inertia by a moving crack. *Phys Rev Lett* 104:114301
- Guerra C, Scheibert J, Bonamy D, Dalmas D (2012) Understanding fast macroscale fracture from microscale post-mortem patterns. *Proc Natl Acad Sci USA* 109:390
- Gumbsch P, Zhou SJ, Holian BL (1997) Molecular dynamics investigation of dynamic crack stability. *Phys Rev B* 55:3445
- Henry H (2008) Study of the branching instability using a phase field model of inplane crack propagation. *EPL* 83:16004
- Henry H, Levine H (2004) Dynamic instabilities of fracture under biaxial strain using a phase field model. *Phys Rev Lett* 93:105504
- Holloway DG (1968) The fracture of glass. *Phys Educ* 3:317
- Hull D (1999) *Fractography: observing, measuring and interpreting fracture surface topography*. Cambridge University Press, Cambridge
- Irwin GR, Kies JA (1952) Fracturing and fracture dynamics. *Weld J Res Suppl* 31:95

- Kalthoff JF, Winkler S, Beinert J (1976) Dynamical stress intensity factors for arresting cracks in dbc specimens. *Int J Fract* 12:317
- Karihaloo BL, Xiao QZ (2001) Higher order terms of the crack tip asymptotic field for a wedge-splitting specimen. *Int J Fract* 112:129
- Kies JA, Sullivan AM, Irwin GR (1950) Interpretation of fracture markings. *J Appl Phys* 21:716
- Kobchenko M, Panahi H, Renard F, Dysthe KD, Malthe-Sørenssen A, Mazzini A, Scheibert J, Jamtveit B, Meakin P (2011) 4D imaging of fracturing in organic-rich shales during heating. *J Geophys Res* 116:B12201
- Livne A, Bouchbinder E, Svetlizky I, Fineberg J (2010) The near-tip fields of fast cracks. *Science* 327:1359
- Moore DE, Lockner DA (1995) The role of microcracking in shear-fracture propagation in granite. *J Struct Geol* 17:95
- Murali P, Guo T, Zhang Y, Narasimhan R, Li Y, Gao H (2011) Atomic scale fluctuations govern brittle fracture and cavitation behavior in metallic glasses. *Phys Rev Lett* 107:215501
- Panahi H, Kobchenko M, Renard F et al (2012) A 4D Synchrotron X-ray-tomography study of the formation of hydrocarbon-migration pathways in heated organic-rich shale. *SPE J. SPE-162939-PA* (in press; posted 27 November 2012)
- Persson BNJ, Brener EA (2005) Crack propagation in viscoelastic solids. *Phys Rev E* 71:036123
- Prades S, Bonamy D, Dalmas D, Bouchaud E, Guillot C (2005) Nano-ductile crack propagation in glasses under stress corrosion: spatiotemporal evolution of damage in the vicinity of the crack tip. *Int J Solids Struct* 42:637
- Rabinovitch A, Bahat D (2008) Mirror-mist transition in brittle fracture. *Phys Rev E* 78:067102
- Rabinovitch A, Belizovsky G, Bahat D (2000) Origin of mist and hackle patterns in brittle fracture. *Phys Rev B* 61:14968
- Ravi-Chandar K (1998) Dynamic fracture of nominally brittle materials. *Int J Fract* 90:83
- Ravi-Chandar K (2004) Dynamic fracture. Elsevier Ltd, Amsterdam
- Ravi-Chandar K, Knauss WG (1984) An experimental investigation into dynamic fracture-ii microstructural aspects. *Int J Fract* 25:65
- Ravi-Chandar K, Yang B (1997) On the role of microcracks in the dynamic fracture of brittle materials. *J Phys Mech Solids* 45:535
- Regel VR (1951) O mekhanizme kheupkogo razusheniya plastmass. *Zhurnal Tekhnicheskoi Fiziki* 21:287
- Rice JR (1968) A path independent integral and the approximate analysis of strain concentration by notches and cracks. *J Appl Mech* 35:379
- Rosakis AJ, Duffy J, Freund LB (1984) The determination of dynamic fracture toughness of aisi 4340 steel by the shadow spot method. *J Mech Phys Solids* 32:443
- Rountree CL, Kalia RK, Lidorikis E, Nakano A, Brutzel LV, Vashishta P (2002) Atomistic aspects of crack propagation in brittle materials: multimillion atom molecular dynamics simulations. *Annu Rev Mater Res* 32:377
- Rountree CL, Bonamy D, Dalmas D, Prades S, Kalia RK, Guillot C, Bouchaud E (2010) Fracture in glass via molecular dynamics simulations and atomic force microscopy experiments. *Phys Chem Glass Eur J Glass Sci Technol B* 51:127
- Scheibert J, Guerra C, Célarié F, Dalmas D, Bonamy D (2010) Brittle/quasi-brittle transition in the dynamic fracture of nominally brittle materials: an energetic signature. *Phys Rev Lett* 104:045501
- Sharon E, Fineberg J (1999) Confirming the continuum theory of dynamic brittle fracture for fast cracks. *Nature* 397:333
- Smekal (1953) Zum bruchvorgang bei sprödem stoffverhalten unter ein- and mehrachsigen beanspruchungen. *Osterr Ing Arch* 7:49
- Spatschek R, Hartmann M, Brener E, Müller-Krumbhaar H, Kassner K (2006) Phase field modeling of fast crack propagation. *Phys Rev Lett* 96:015502
- Washabaugh PD, Knauss W (1994) A reconciliation of dynamic crack velocity and rayleigh wave speed in isotropic brittle solids. *Int J Fract* 65:97